Sensors and Actuators A 322 (2021) 112625

Contents lists available at ScienceDirect

Sensors and Actuators A: Physical

journal homepage: www.elsevier.com/locate/sna

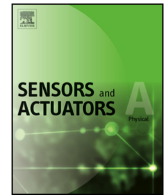

Enhancing the device performance of SiNP array/$PtTe_2$ heterojunction photodetector by the light trapping effect

Xiao-Wei Tong[a], Jun-Jie Wang[a], Jia-Xiang Li[a], Xue-Feng Hu[b,*], Di Wu[c], Lin-Bao Luo[a,*]

[a] School of Electronic Science and Applied Physics, Hefei University of Technology, Hefei, 230009, China
[b] Academy of Optoelectronic Technology, National Engineering Laboratory of Special Display Technology, Hefei University of Technology, Hefei, 230009, China
[c] School of Physics and Microelectronics, Zhengzhou University, Zhengzhou, 450052, China

ARTICLE INFO

Article history:
Received 25 October 2020
Received in revised form 31 January 2021
Accepted 9 February 2021
Available online 11 February 2021

Keywords:
Two-dimensional materials
Transition metal dichalcogenides
Photodetectors
Image sensors
Heterojunctions

ABSTRACT

In this study, we have demonstrated the fabrication of a highly sensitive photodetector, which was based on Si nano-pillar (SiNP) array/$PtTe_2$ heterojunction that can work under a self-powered mode of operation. The as-fabricated heterojunction exhibits the obvious current rectifying behavior with a rectification ratio of 6×10^3 at a bias voltage of ±1 V. Moreover, it displayed an intriguing photoelectric ability to a wide range of illumination from ultraviolet to near-infrared light. Under light illumination at 980 nm, the photodetector exhibits a responsivity of 0.71 A W^{-1}, a specific detectivity of 2.81×10^{11} Jones, and an external quantum efficiency of 89.9 %, respectively. More importantly, the device has a fast response speed of τ_{raise}/τ_{fall} of 6.21 / 26.3 μs. Thanks to the light trapping effect of the surficial nanostructure, the SiNP array effectively improves the absorption of the heterojunction, and therefore enhances the detecting performance of the device. Moreover, the device is able to record a near-infrared letter with acceptable resolution. All of these results suggest that present two-dimensional material may have potential application in future high-performance optoelectronic devices.

© 2021 Elsevier B.V. All rights reserved.

1. Introduction

Since the discovery of graphene (Gr) in 2004 [1], two-dimensional materials have intrigued a tremendous interest all over the world. Owing to their fantastic electric and photoelectric properties [2], such as high carrier mobility [3,4], prominent mechanical flexibility [5], and tunable bandgap [6], two-dimensional materials have exhibited promising potential in a variety of optoelectronic devices (e.g. solar cells, light emitting dioxides, photodetectors, lasers, and photoelectric field-effect transistors) [7–9], especially for light detection due to its incredible value in the military surveillance, space-based warning, industry automation, remote control, and so on [10]. In recent years, two-dimensional transition metal dichalcogenides (2D TMDs) with geometry of a van der Waals heterojunction exhibit remarkable performance in optoelectronics [11]. Among various 2D TMDs, group-10 metal dichalcogenides are capable of realizing large-scale and controllable fabrication of high-performance optoelectronic devices [12,13] because of their facile synthesis methods and excellent photoelectric properties [14]. For example, group-10 2D TMDs/Si heterojunction device can be easily constructed by directly transferred or fabricated on the silicon surface, while traditional Si p − n (or p − i − n) junctions often involve the complicated fabrication processes for high-temperature ion diffusion or costly implantation procedures. In addition, the absence of dangling bonds on naturally terminated surfaces is more beneficial to their ambient stability, which might help protect a group-10 TMDs device from surface-induced performance degradation [15].

$PtTe_2$ as a representative of 2D TMDs has predicted to be a very important candidate for various optoelectronics [16] due to the existence of type-II Dirac fermions [17,18]. Considering the fabulous compatibility with present semiconductor technology, it demonstrates potential applications in the heterojunction photodetectors [19], image sensors [20], and even silicon-based integrated optoelectronic systems [21]. In this work, we introduced a high-performance photodetector by combining group-10 TMDs of $PtTe_2$ with SiNP array, which exhibits great advantages for photoelectric device on account of the periodic structure that effectively suppress the reflection of incident light, and increase the effective illumination area. In addition, the large surface-to-volume ratio can prolong the lifetime of photo-excited carriers, shorten carriers

* Corresponding authors.
E-mail addresses: xuefeng.hu@hfut.edu.cn (X.-F. Hu), luolb@hfut.edu.cn (L.-B. Luo).

https://doi.org/10.1016/j.sna.2021.112625
0924-4247/© 2021 Elsevier B.V. All rights reserved.

transiting time, and ultimately enhance the photoelectric conversion efficiency of optoelectronics [22–24]. The as-fabricated device exhibits remarkable photoelectric conversion ability in a wide spectrum from ultraviolet to near-infrared light. Under 980 nm light illumination, the responsivity (R), specific detectivity (D^*) and external quantum efficiency (EQE) are estimated to be 0.71 A W^{-1}, 2.81 × 10^{11} Jones, and 89.9 %, respectively at zero bias. More importantly, the device also displays a short response time (τ_{raise}/τ_{fall}) of 6.21/ 26.3 μs. What is more, the photoelectric properties exhibit nearly invariant after storage in air for 3 months, indicating a better ambient stability in nature circumstance. Considering the good optoelectronic properties and easy fabrication, the present SiNP array/$PtTe_2$ core/shell heterojunction can be regarded as a promising building block for assembly of high-performance optoelectronic devices.

2. Experimental section

2.1. Materials synthesis and device fabrication

In this study, platinum telluride was synthesized by directly in-situ tellurization of Pt film. In brief, a lightly doped silicon substrate (1–10 Ω cm) with 300 nm silicon dioxide insulator layer was treated with ultrasonic cleaning in acetone, alcohol, and deionized water for 15 min, respectively. The selected area of SiO_2 was removed by an etching solution (hydrofluoric acid, ammonium fluoride, and ultrapure water) without positive photoresist as a protecting layer. The selected area of Si was loaded a single layer close-packed polystyrene (PS) spheres by a slow-pulling method. The as-assembled PS spheres were treated by the reactive ion etching process with oxygen plasma, which results in homogenous dispersed PS spheres with reduced diameters. After the deposition of the 30 nm silver film by the electron-beam evaporation, the sample was immersed into a mixed etching solution (the volume ratio of hydrofluoric acid, hydrogen peroxide, and distilled water was 10:1:40) for 20 min. The photoresist was removed by acetone, and then the sample was washed by ethanol and deionized water, respectively. After drying by nitrogen gas, 10 nm platinum film was deposited onto the selected area of the sample, with the assistance of lithography technology. The platinum-loaded sample was placed at the center zone of the furnace and tellurium (Te) powder (99.99 %) was placed in the upstream side. The furnace was heated to 873 K for 120 min, and then naturally cooled to room temperature. The whole tellurization procedure was protected by argon gas with the flow rate of 90 SCCM. 50 nm gold film was deposited onto platinum telluride as top electrodes. In-Ga alloy, as bottom electrodes, was employed to connect the back side of the sample and a printed circuit board (PCB).

2.2. Materials characterization and device analysis

The structure of the $PtTe_2$ film was analyzed by Raman spectrometer (Horiba Jobin Yvon, LabRAM HR800) and X-ray diffractometer (Rigaku D/max-rB). The morphology and EDS of the $PtTe_2$ film were characterized by field-emission scanning electron microscopy (FESEM, SU8010) and high-resolution transmission electron microscopy (HRTEM) (JEM-2100 F). The absorption of the $PtTe_2$ film was characterized by ultraviolet-visible-near-infrared spectrophotometer (CARY 5000). The chemical composition of the $PtTe_2$ film was determined by X-ray photoelectron spectroscopy (XPS) analysis (Thermo, ESCALAB250Xi). The electrical measurements of the SiNP array/$PtTe_2$ core/shell heterojunction was tested by the home-made system containing a semiconductor characterization system (Keithley 4200) and a series of lasers (Thorlabs Company). The laser diode driven by the function generator and GHz oscilloscope (Tektronix, TDS2012B) were employed to characterize the response speed.

2.3. Theoretical simulation

The energy density distribution of the electric field of the SiNP array/$PtTe_2$ heterojunction was analyzed by using the finite element method (FEM). Considering the periodic structure, the simulation of the electric field distribution was only performed for two-unit cells. Plane waves are used to simulate the incident light on top of the structure. During the simulation, structural parameters of the model were extracted from the SEM image of the sample, in which r_0 = 175 nm, r_1 = 220 nm, H_0 =3500 nm, H_1 = 3530 nm, and P = 700 nm, respectively. Here, P denotes the period of the array, and r_0 (r_1) and H_0 (H_1) represent the radius and height of SiNP (SiNP/$PtTe_2$), respectively.

3. Results and discussion

The SiNP array/$PtTe_2$ core/shell heterojunction (Fig. 1a) was assembled by a feasible procedure including Ag-assisted etching of Si, direct e-beam evaporation of Pt, and subsequent facile tellurization process. The detailed schematic diagram of the fabrication process is shown in Fig. S1. The morphologies of both SiNP array (Fig. 1b-c) and SiNP array/$PtTe_2$ core/shell heterojunction (Fig. 1d & e) were primarily studied by field-emission scanning electron microscopy (FESEM). It is obviously observed that the SiNP array is perpendicular to the surface with uniform radius of ∼350 nm, height of ∼3 μm, and interval of ∼150 nm. What is more, the $PtTe_2$ film with thickness of ∼50 nm is actually composed of a variety of distinguishable clusters, which form a continuous layer throughout the SiNP array. Such a unique device geometry will facilitate not only light harvesting, but also for electron-hole pairs separation, which will be beneficial for photodetection application [21]. From analysis of HRTEM image (Fig. 1f), the $PtTe_2$ sample is polycrystalline, and the grain size is about several to tens nanometers. The TEM image and elemental mapping images suggest that both Pt and Te elements are evenly distributed onto the SiNP array surface (Fig. 1g). According to the energy-dispersive X-ray spectroscopy (EDS) in Fig. S2a, the atomic ratio of Pt/Te element is estimated to be 33.6:66.4, which is ideally close to the stoichiometric proportion of $PtTe_2$. More characterizations (Raman spectrum, XRD pattern, XPS spectra, and HRTEM image) of as-synthesized $PtTe_2$ were provided in supporting information (Fig. S2b-f), which is consistent with previously reported results [25–27].

Fig. 2a depicts the I–V characteristic of the SiNP array/$PtTe_2$ heterojunction in the dark. Obviously, this heterojunction exhibits a typical rectifying behavior, with a rectification ratio as high as 6 × 10^3 within ±1 V, which is higher than previously reported heterojunctions with similar structures ($PdSe_2$/pyramid Si [22], and Si nanowires/Cs doped $FAPbI_3$ [28]). The remarkable rectifying characteristic is originated from SiNP array/$PtTe_2$ heterojunction, since good Ohmic contact is formed in both the Au-$PtTe_2$ (Fig. S3) and In/Ga-Si structures [22]. When the device was shined by 980 nm light illumination, the I–V curve exhibits an obvious photovoltaic effect (Fig. 2b). The open-circuit voltage (V_{OC}) and short-circuit current (I_{SC}) are estimated to be 0.36 V and 3.58 μA, respectively. The typical photovoltaic effect endows the heterojunction with a self-driving operational mode. The mechanism of this behavior is originated from the fact that the work function (E_F) of $PtTe_2$ is lower than that of n-type Si. When they are in contact with each other, the electrons in the interface of Si will diffuse to $PtTe_2$ to make the E_F of the former in line with that of the latter, further inducing the energy band of Si interface to bend upward. Consequently, a built-in electric field is formed at the $PtTe_2$/Si interface, as illus-

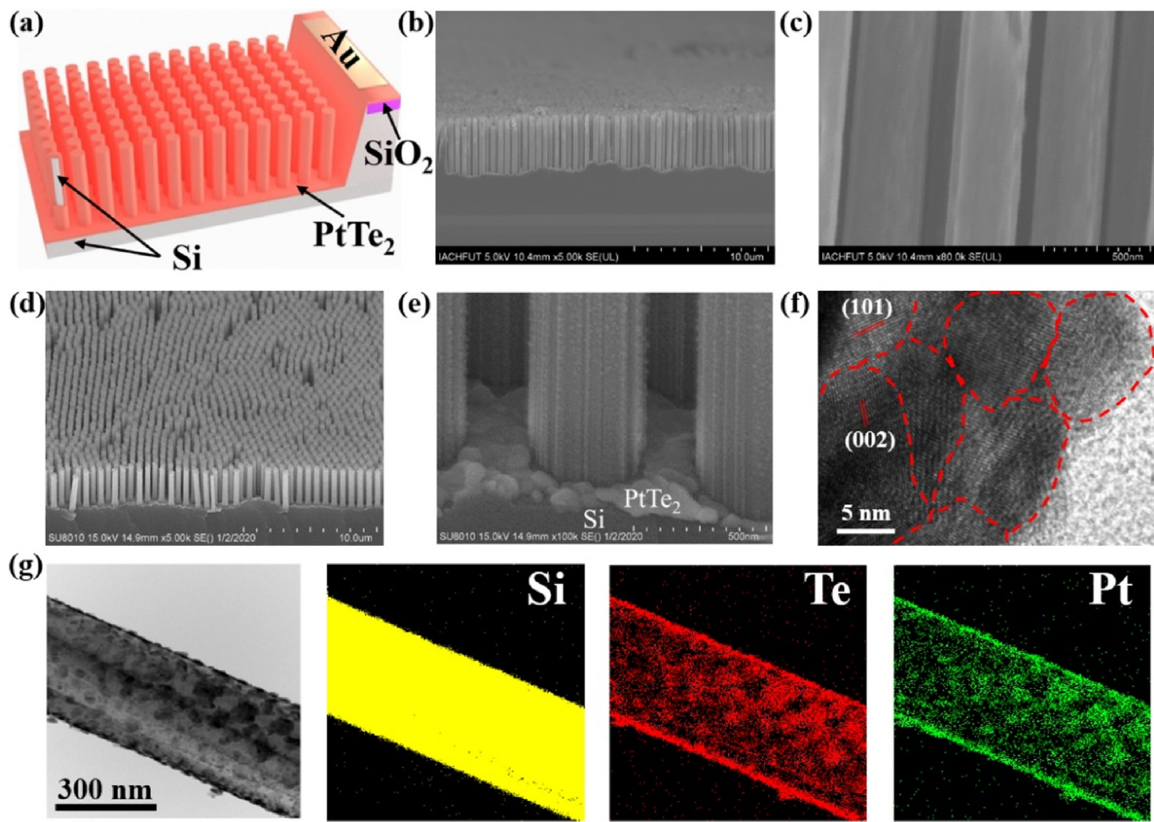

Fig. 1. (a) Schematic diagram of SiNP array/$PtTe_2$ heterojunction. (b) and (c) FESEM images of SiNP array. (d) and (e) FESEM images of SiNP array/$PtTe_2$ core-shell structure. (f) The HRTEM image of the shell of $PtTe_2$. (g) Elemental mapping images of silicon, platinum, and tellurium.

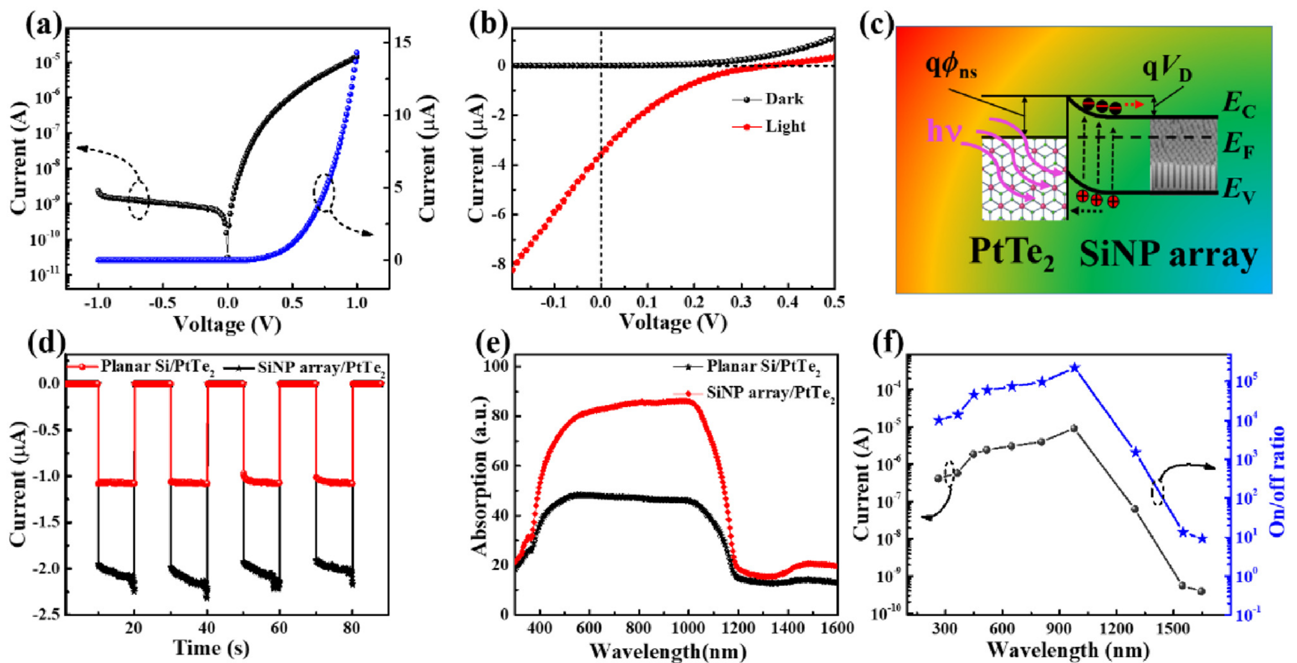

Fig. 2. (a) *I-V* characteristic of the SiNP array/$PtTe_2$ heterojunction in the dark. (b) *I-V* curves of the heterojunction photodetector in darkness and under 980 nm light illumination. (c) Energy band diagram of the SiNP array/$PtTe_2$ heterojunction under light illumination at zero bias. (d) Photo-response of the photodetector under 980 nm light illumination at zero bias with light intensity of 360 $\mu W\ cm^{-2}$. (e) Experimental absorption spectra of both planar Si/$PtTe_2$ and SiNP array/$PtTe_2$ heterojunction devices. (f) Photocurrent and on/off ratio of the heterojunction photodetector with different wavelengths at zero bias.

trated in Fig. 2c. The photo-response characteristics under 980 nm light illumination are plotted in Fig. 2d, the vertical rise and fall slopes illustrate that the core/shell heterojunction can rapidly separate the photoexcited electron-hole pairs. Specifically, the on/off ratio can easily approach 10^5 at zero bias, which is superior to previously reported similar heterojunction ($PtSe_2$/Si [29], Gr/Si [30],

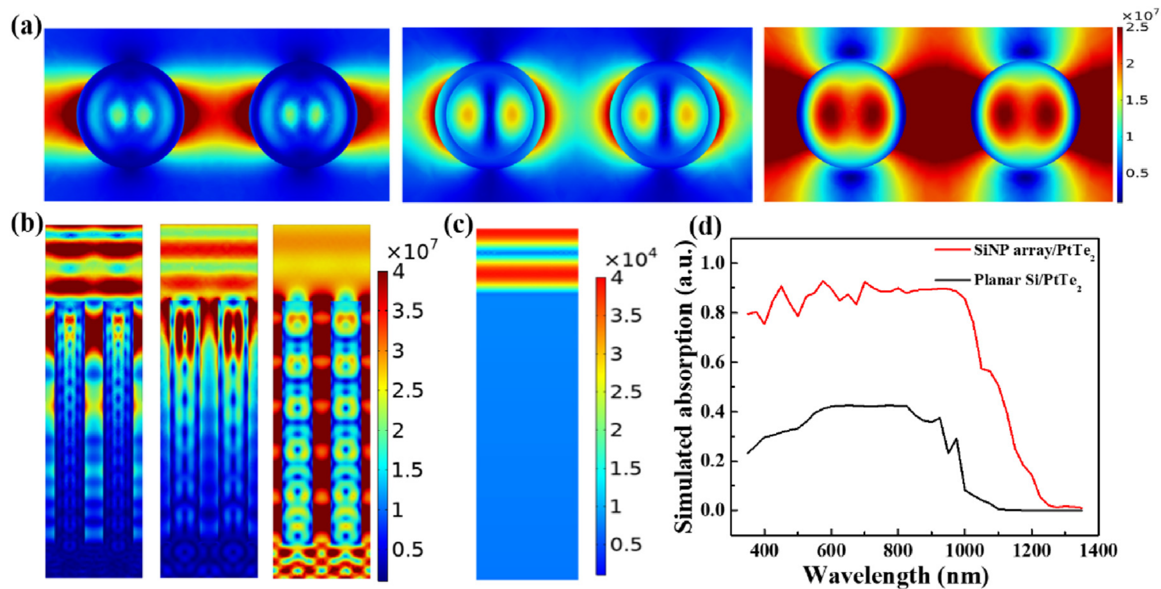

Fig. 3. Electric field intensity plots of leaky mode resonances of SiNP array/$PtTe_2$ at λ = 650 nm, λ = 980 nm, and λ = 1300 nm, which corresponds to the HE_{13} and HE_{12} modes, respectively. (a) The top row illustrates the top view of $|E(r)|^2$ at the x-y plane, while the bottom (b) shows a side view at the x-z plane. (c) Electric field density distribution of the planar Si/$PtTe_2$ under 980 nm illumination. (d) Simulated absorption curves of the SiNP array/$PtTe_2$ and planar Si/$PtTe_2$.

and $CsBi_3I_{10}$/Si [31]), and further suggests the good carrier separation and collection capability of the core/shell heterojunction. Both the separation speed and efficiency of the heterojunction further demonstrate a low level of defect states existed in the interface between SiNP array and $PtTe_2$. What is more, the photocurrent of the SiNP array/$PtTe_2$ heterojunction is 1.94 times of that of planar Si/$PtTe_2$ based device under the same intensity of light illumination (Fig. 2d). The enhancement of photo-response can be interpreted by the light trapping effect of the SiNP array: The nanostructure of the SiNP array/$PtTe_2$ heterojunction can effectively suppress the reflection of incident light by substantially increasing the optical path [22], which leads to increase in absorption from 46 % to 86 % in comparison to the planar Si/$PtTe_2$, as shown in Fig. 2e.

The photo-response of the SiNP array/$PtTe_2$ heterojunction was found to be strongly related to the wavelength of incident light. As shown in Fig. S4a-b, obvious photovoltaic behavior is observed in ultraviolet-visible-near-infrared region. The strongest response is located at the wavelength of 980 nm. Under light illumination with different wavelengths, the response of the heterojunction can be quickly switched at zero bias (Fig. S4c). The evolution of the photocurrent and on/off ratio as a function of wavelength are summarized in Fig. 2f. It can be seen that the photocurrent increases slowly from 0.41 μA at the wavelength of 265 nm to 8.9 μA at the wavelength of 980 nm, and subsequently dramatically decreases to 0.37 nA at the wavelength of 1650 nm. Similarly, the on/off ratio gradually rises from 10^4 to 2.2×10^5, and then rapidly drops to 9.25. Such a tendency kept in agreement with the V_{OC} of device in the *I–V* curves. Considering the fact that the $PtTe_2$ in this study exhibits typical semimetal characteristics, the above peak response at the wavelength of 980 nm is mainly due to the contribution from Si, which has absorption edge at nearly the same wavelength. Understandably, the observed photoelectric behavior at near bias voltage is related to carrier separation by built-in electric field at the interface of SiNP array/$PtTe_2$ heterojunction [32,33]. During this photoelectric process, only photons with energy higher than the bandgap of Si can efficiently generate electron-hole pairs. That is why when wavelength is increased to longer values i.e. 1650 nm, very low photocurrent was formed [34].

In order to shed light on the relatively good performance of the above SiNP array/$PtTe_2$ heterojunction, we simulated the electric field distributions by using FEM numerical simulation. Fig. 3a-b are the electric field distributions in the x–y and x–z sections at the incident wavelengths of 650, 980, and 1300 nm. We can find from the x–y section that the incident lights at different wavelengths form different leaky resonance modes [35]. Among them, 650 nm light corresponds to the HE_{13} mode, 980 and 1300 nm lights correspond to the HE_{12} mode, and 1300 nm light is coupled to the waveguide mode supported by NPs with higher efficiency [36]. Furthermore, it can be seen from the x–z section that, for incident lights with the wavelengths of 650 and 980 nm, the intensities of the incident lights along the waveguide inside the NPs have a significant attenuation during the propagation due to the absorption loss of the Si NPs. On the contrary, there is no obvious attenuation along the waveguide at 1300 nm, indicating that the silicon has nearly no absorption in this region. All these results are in full agreement with the experimental and simulated absorption spectra. Fig. 3c shows a planar Si/$PtTe_2$ structure. The electric field intensity inside and near the surface of the NPs is much greater than that of the planar structure under the same conditions. Fig. 3d compares the absorption efficiency curves of the SiNP array/$PtTe_2$ and planar Si/$PtTe_2$ through simulation. Obviously, the simulation result is in good agreement with the experimental ones. Therefore, the enhanced interaction between the NPs and light greatly improves the absorption of the device. As a matter of fact, the above phenomenon can be understood from the following two aspects. On one hand, the NPs structure not only has a large effective device area to improve the transport capacity of photo-generated carriers, but also makes the light continuously reflect between the NPs due to its periodic properties, which forms a light-trapping mode and increases the utilization efficiency of photons [28]. On the other hand, the NPs can be regarded as a miniature resonator, which can form the HE_{1m} transverse resonance mode [37]. The HE_{12} and HE_{13} resonance modes distributing in and around the NPs array lead to the enhancement of local field, and ultimately increase the absorption of some specific incident lights.

Apart from the wavelength, the photoresponse also depends on the intensity of incident light. Fig. 4a shows the *I–V* curves of the heterojunction device under 980 nm light illumination with a series of intensities from 0.0684 to 11.88 μW cm^{-2}. Apparently, the photoresponse at both zero and reverse bias are enhanced with

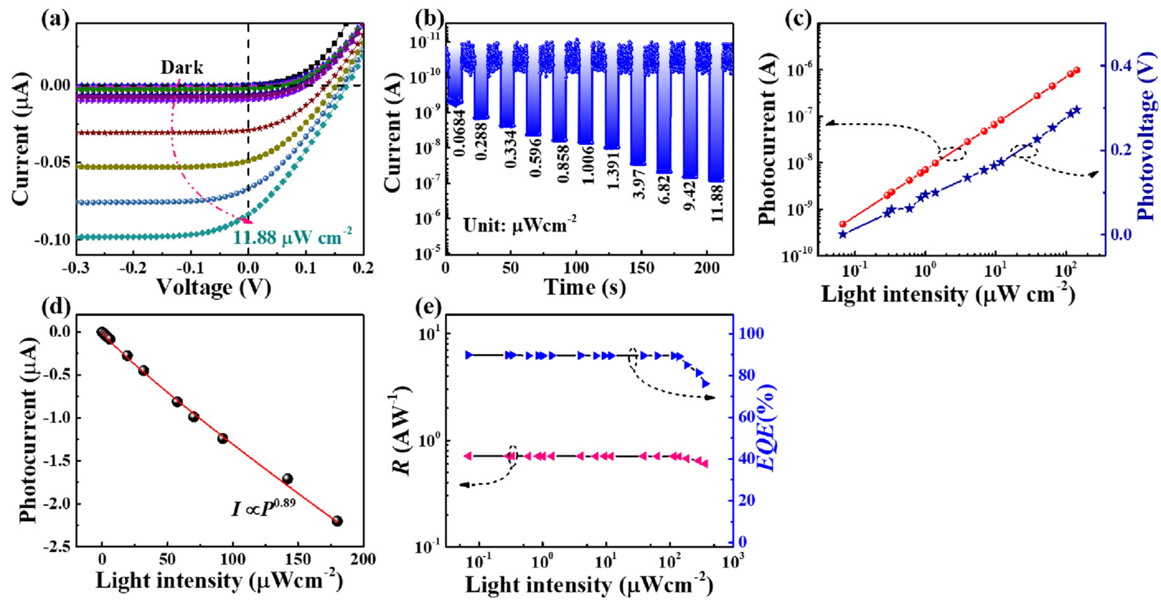

Fig. 4. (a) *I-V* characteristics of the SiNP array/$PtTe_2$ heterojunction in darkness and under 980 nm light illumination with varied intensities. (b) Photo-response of the photodetector under 980 nm illumination with different intensities. (c) Photocurrent and photovoltage of the photodetector under 980 nm illumination with different intensities. (d) Photocurrent of the photodetector as a function of incident-light intensity at zero bias. (e) Both *R* and *EQE* of the device as a function of light intensity.

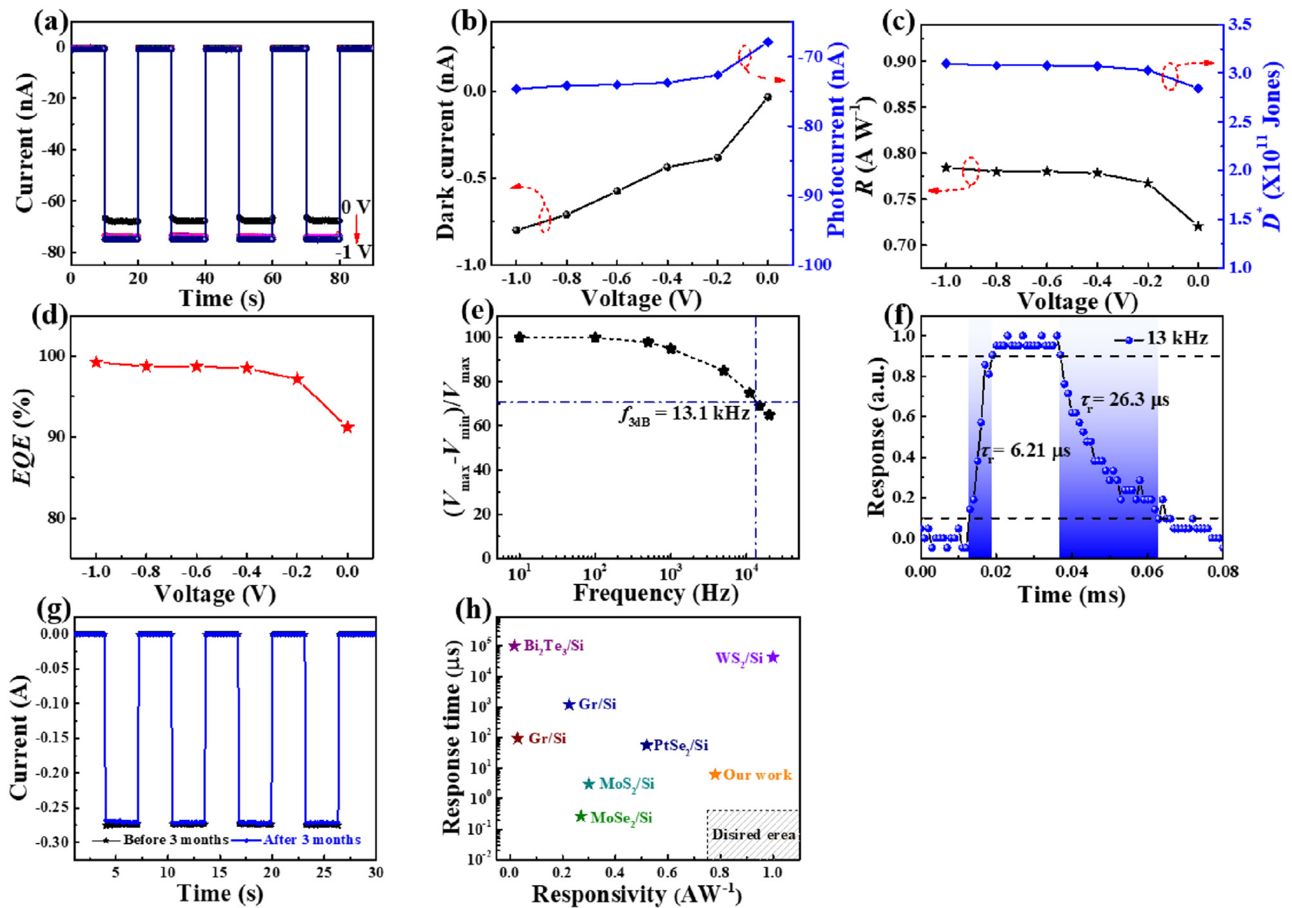

Fig. 5. (a) Photoresponse of the photodetector at zero and different reverse bias voltages. (b) Both dark current and photocurrent of the device as a function of reverse bias voltage. (c) Both responsivity and specific detectivity of the device as a function of reverse bias voltage. (d) *EQE* of the device as a function of reverse bias voltage. (e) Relative balance (V_{max}-V_{min})/V_{max} versus switching frequency of incident light. (f) A single enlarged cycle of photoresponse for estimating rise and fall times. (g) Photoresponse of the device was tested before and after storage in air for three months. (h) Comparison of key parameters of the device in this work with previously reported photodetectors with similar geometries.

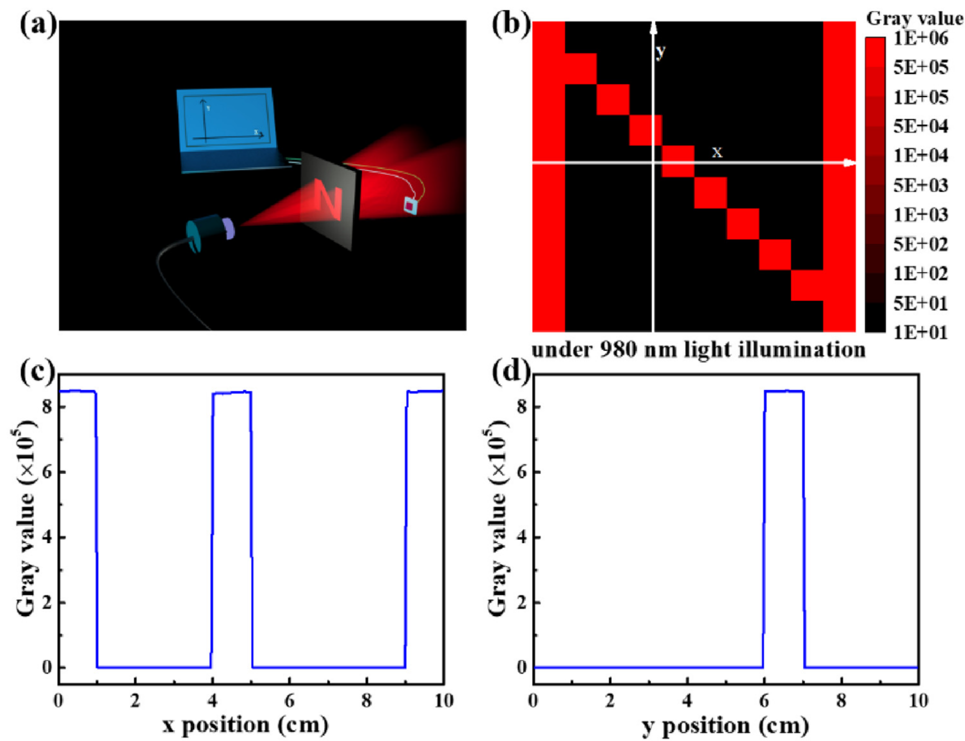

Fig. 6. (a) Schematic diagram of the measurement for the image sensing application. (b) Corresponding images of "N" letter under 980 nm light illumination. Gray values as a function of x position (c) and y position (d) under patterned 980 nm light illumination.

the intensity increasing, which can be ascribed to the reason that the larger number of photons at a higher intensity contributes to the generation of more carriers. The corresponding photoresponse curves are plotted in Fig. 4b (0.0684–11.88 μW cm^{-2}) and Fig. S5 (11.88–140.3 μW cm^{-2}), in which the corresponding photocurrent can be swiftly switched between on (light illumination) and off (dark) states, suggesting that the device can effectively detect the illumination with a large range of intensities. The photocurrent nearly increases monotonously from 0.48 nA to 0.99 μA when the light intensity ascends from 0.0684–140.3 μW cm^{-2}. Similarly, the corresponding photovoltage gradually increases from 0.001 to 0.296 V. The relationship of the photocurrent and intensity of the incident light can be further quantitatively described as a formula of $I_{ph}=AP^{\theta}$, where A is a parameter for light, P is the power of the incident light, and θ is the exponent of photo-response and indicates the linear relationship of power densities and photocurrents, respectively. As the fitting result shown in Fig. 4d, θ is estimated to be 0.89. This result is very close to the ideal value of 1, indicative of a low level of trap states in the heterojunction. In order to quantitatively evaluate the performance of the SiNP array/$PtTe_2$ core/shell heterojunction photodetector, key parameters, like responsivity (R), specific detectivity (D^*) and external quantum efficiency (EQE) were employed, which can be estimated by the following formulas [38,39,49]:

$$R = \frac{I_{light} - I_{dark}}{P_{\lambda} S} \quad (1)$$

$$D^* = \frac{RS^{1/2}}{(2qI_{dark})^{1/2}} \quad (2)$$

$$EQE = \frac{hcR}{q\lambda} \quad (3)$$

Where P_{λ} is the intensity of incident light, S is the effective illumination area (0.01 cm^2), λ is the wavelength of incident light, q is the value of electron charge, h is the Planck's constant, c is the speed of light, and I_{light} and I_{dark} are the currents of the device under light illumination and in the dark, respectively. According to above equations and the measurements of the photodetector under 980 nm light illumination with an intensity of 0.0684 μW cm^{-2} at zero bias, R, D^*, and EQE are calculated to be 0.71 A W^{-1}, 2.81 × 10^{11} Jones, and 89.9 %, respectively. As shown in Fig. 4e, both R and EQE keep nearly unchanged with the intensity in the range of 0.0684–140.3 μW cm^{-2}, and then obviously decrease with the light intensity further increasing. This finding can be understood as follows: When the photodetector was shined by weak light, all the photo-generated carriers will be separated by the built-in electric field, leading to a linear relationship between the photocurrent and light intensity [40]. However, when the light intensity keeps increasing, more and more carriers were generated in the depletion. In the case, due to strong carrier recombination, part of the photo-generated carrier can be effectively separated by the built-in electric field. Consequently, the photocurrent cannot keep the linear changing with the intensity increasing. As a result, R keeps unchanged at weak intensity, but it decreases at high intensity

The influence of the bias voltage on the properties of the heterojunction is also discussed. The photo-response of the photodetector under 980 nm light illumination with the intensity of 9.42 μW cm^{-2} at zero and different reverse bias voltages are illustrated in Fig. 5a-b. One can easily find that the device exhibits typical detecting ability at both zero and reverse bias. The dark current obviously increases from 2.1 × 10^{-11} A at zero bias to 3.8 × 10^{-10} A at reverse bias voltage of -0.2 V, and then slowly increases to 8.0 × 10^{-10} A with the reverse voltage increasing to −1 V, while the photocurrent obviously enhances from 67.9 to 72.7 nA with the voltage reinforcing from 0 to -0.2 V, and remains nearly unchanged in the bias voltage range from -0.2 to −1 V. Since the reverse bias voltage has the same direction as that of the built-in electric field, application of a reverse bias will intensify the intensity of the electric field which will facilitate the separation of photo-generated carriers and extend the depletion region. For this reason, R, D^*, and EQE are improved

from 0.71 A W^{-1}, 2.81 × 10^{11} Jones, and 89.9 %, to 0.78 A W^{-1}, 3.09 × 10^{11} Jones, and 99.2 %, respectively, when the bias voltage was decreased from zero to −1 V, as summarized in Fig. 5c-d. These Figure-of-merits values are close to or even superior to that of the heterojunction with similar structures (Si nanowires/C quantum dots [22], and Si nanowires/Cs doped $FAPbI_3$ [28]). The response time of the device was further studied by the home-made system consisting of an oscilloscope, a laser diode, and a function generator. Fig. 5e and S6 show the relative balance (V_{max}-V_{min})/V_{max} of the device as a function of signal frequencies (800 Hz to 15 kHz). The 3 dB bandwidth ((V_{max}-V_{min})/V_{max} decreases from 100 to 70.7 %) is estimated to be 13.1 kHz. Fig. 5f presents an individual cycle of the photoresponse at 13 kHz, the rise time (the photoresponse increases from 10 % to 90 %) and fall time (the photoresponse decreases from 90 % to 10 %) are evaluated to be 6.21 and 26.3 μs, respectively. Moreover, the heterojunction can stably work under light impulses for more than 20 min (Fig. S7) with no obvious degradation in performance. In addition, after the storage in atmosphere for 3 months, as shown in Fig. 5g, the photoresponse of the heterojunction degrades by less than 1.2 % under the same intensity of 980 nm light illumination, these results suggest the good device reproducibility and ambient stability, which is very important for the potential application in future optoelectronics. Fig. 5h summarizes some of the key parameters of the present devices and other devices with similar geometries: The responsivity of this device is slightly poorer than that of WS_2/Si [41], but are much better than previously reported heterojunction devices like $PtSe_2$/Si [42], Bi_2Te_3/Si [43], Gr/Si [44], $MoSe_2$/Si [45], MoS_2/Si [46], and Gr/Si [47]. On the other hand, the response speeds are faster than that of other devices with analogical structures except for $MoSe_2$/Si [45] and MoS_2/Si [46].

To further study the detection capability of the self-driving heterojunction detector, a home-made imaging system was constructed. As shown in Fig. 6a, a shadow mask with a hollow character of N was employed to pattern the light. The photodetector was fixed onto a home-made translation stage with moving orbit along horizontal (x) and vertical (y) directions. Under parallel light beams with different wavelengths and the same intensity, a semiconductor characterization system (Keithley 4200) was applied to record the time dependent current signal of the device (The position value is equal to time multiplied by speed, and the gray value is equal to current divided by minimal dark current). From the images shown in Fig. 6b-d and S8, one can see that the imaging system exhibits the highest sensitivity to 980 nm light. The gray value ratios of 980 nm/265 nm, 980 nm/650 nm, and 980 nm/1550 nm are estimated to be 22.1, 3.1, and 1.6 × 10^4, respectively. It also indicates that this imaging system has a capability to roughly distinguish different wavelengths of lights [48].

4. Conclusions

In summary, we have successfully fabricated a highly sensitive heterojunction photodetector with brilliant detection capability. The as-fabricated SiNP array/$PtTe_2$ core/shell heterojunction displayed a remarkable rectifying effect with the excellent rectification ratio of 6.0 × 10^3 at a bias voltage of ±1 V. Moreover, the responsivity, specific detectivity, and external quantum efficiency were estimated to be 0.78 A W^{-1}, 3.09 × 10^{11} Jones, and 99.2 %, respectively, which are better than many previously reported heterojunction devices with similar geometries. Such relatively good optoelectronic property, along with remarkable stability, and excellent images sensing characteristics render the present SiNP array/$PtTe_2$ core/shell heterojunction promising building blocks for assembly of high-performance optoelectronic devices in future.

Author statement

All authors have seen and approved the final version of the manuscript being submitted.

Declaration of Competing Interest

The authors declare no conflict of interest.

Acknowledgements

This work was supported by the National Natural Science Foundation of China (NSFC, Nos. 62074048), the Fundamental Research Funds for the Central Universities (JZ2018HGXC0001), and the Open Foundation of Anhui Provincial Key Laboratory of Advanced Functional Materials and Devices (4500-411104/011).

Appendix A. Supplementary data

Supplementary material related to this article can be found, in the online version, at doi:https://doi.org/10.1016/j.sna.2021.112625.

References

[1] K.S. Novoselov, A.K. Geim, S.V. Morozov, D. Jiang, Y. Zhang, S.V. Dubonos, I.V. Grigorieva, A.A. Firsov, Science 306 (2004) 666–669.
[2] K.F. Mak, J. Shan, Nat. Photon. 10 (2016) 216–226.
[3] K.C. Lee, S.H. Yang, Y.S. Sung, Y.M. Chang, C.Y. Lin, F.S. Yang, M.J. Li, K.J. Watanabe, T. Taniguchi, C.H. Ho, C.H. Lien, Y.F. Lin,Adv. Funct. Mater. 29 (2019), 1809011.
[4] H.G. Ji, P. Solís-Fernández, D. Yoshimura, M. Maruyama, T. Endo, Y. Miyata, S. Okada, H. Ago,Adv. Mater. 31 (2019), 1903613.
[5] A. Gupta, T. Sakthivel, S. Seal, Prog. Mater. Sci. 73 (2015) 44–126.
[6] S. Susarla, A. Kutana, J.A. Hachtel, V. Kochat, A. Apte, R. Vajtai, J.C. Idrobo, B.I. Yakobson, C.S. Tiwary, P.M. Ajayan,Adv. Mater. 29 (2017), 1702457.
[7] Z. Wang, P. Wang, F. Wang, J.F. Ye, T. He, F. Wu, M. Peng, P.S. Wu, Y.F. Chen, F. Zhong, R.Z. Xie, Z.Z. Cui, L. Shen, Q.H. Zhang, L. Gu, M. Luo, Y. Wang, H.W. Chen, P. Zhou, A.L. Pan, X.H. Zhou, L.L. Zhang, W.D. Hu,Adv. Funct. Mater. 30 (2020), 1907945.
[8] L. Gao, Q.L. Liao, X.K. Zhang, X.Z. Liu, L. Gu, B.S. Liu, J.L. Du, Y. Ou, J.K. Xiao, Z. Kang, Z. Zhang, Y. Zhang,Adv. Mater. 32 (2020), 1906646.
[9] M.S. Long, P. Wang, H.H. Fang, W.D. Hu,Adv. Funct. Mater. 29 (2019), 1803807.
[10] Y. Lu, J. Chen, T.X. Chen, Y. Shu, R.J. Chang, Y.W. Sheng, V. Shautsova, N. Mkhize, P. Holdway, H. Bhaskaran, J.H. Warner,Adv. Mater. 32 (2020), 1906958.
[11] Q.H. Zhao, W.Q. Jie, T. Wang, A. Castellanos-Gomez, R. Frisenda,Adv. Funct. Mater. 30 (2020), 2001307.
[12] W. Zheng, R. Schönemann, N. Aryal, Q. Zhou, D. Rhodes, Y.C. Chiu, K.W. Chen, E. Kampert, T. Förster, T.J. Martin, G.T. McCandless, J.Y. Chan, E. Manousakis, L. Balicas,Phys. Rev. B 97 (2018), 235154.
[13] Y.Y. Gu, H. Cai, J.C. Dong, Y.L. Yu, A.N. Hoffman, C.Z. Liu, A.D. Oyedele, Y.C. Lin, Z.Z. Ge, A.A. Puretzky, G. Duscher, M.F. Chisholm, P.D. Rack, C.M. Rouleau, Z. Gai, X.M. Meng, F. Ding, D.B. Geohegan, K. Xiao,Adv. Mater. 32 (2020), 1906238.
[14] H.J. Xu, J.W. Wei, H. Zhou, J.F. Feng, T. Xu, H.F. Du, C.L. He, Y. Huang, J.W. Zhang, Y.Z. Liu, H.C. Wu, C.Y. Guo, X. Wang, Y. Guang, H.X. Wei, Y. Peng, W.J. Jiang, G.Q. Yu, X.F. Han,Adv. Mater. 32 (2020), 2000513.
[15] Q.J. Liang, Q.X. Wang, Q. Zhang, J.X. Wei, S.X. Lim, R. Zhu, J.X. Hu, W. Wei, C.K. Lee, C.H. Sow, W.J. Zhang, A.T.S. Wee,Adv. Mater. 31 (2019), 1807609.
[16] D.Z. Fu, X.Y. Bo, F.C. Fei, B. Wu, M. Gao, X.F. Wang, M. Naveed, S.A. Shah, H.J. Bu, B.G. Wang, L. Cao, W.Q. Zou, X.G. Wan, F.Q. Song,Phys. Rev. B 97 (2018), 245109.
[17] M.Z. Yan, H.Q. Huang, K.N. Zhang, E.Y. Wang, W. Yao, K. Deng, G.L. Wan, H.Y. Zhang, M. Arita, H.T. Yang, Z. Sun, H. Yang, Y. Wu, S.S. Fan, W.H. Duan, S.Y. Zhou, Nat. Commun. 8 (2017) 257.
[18] A. Politano, G. Chiarello, C.N. Kuo, C.S. Lue, R.J. Edla, P. Torelli, V. Pellegrini, D.W. Boukhvalov,Adv. Funct. Mater. 28 (2018), 1706504.
[19] H. Xu, C. Guo, J.Z. Zhang, W.L. Guo, C.N. Kuo, C.S. Lue, W.D. Hu, L. Wang, G. Chen, A. Politano, X.S. Chen, W. Lu,Small 15 (2019), 1903362.
[20] X. Hu, K.P. Wong, L.H. Zeng, X.Y. Guo, T. Liu, L. Zhang, Q. Chen, X.F. Zhang, Y. Zhu, K.H. Fung, S.P. Lau, ACS Nano 14 (2020) 6276–6284.
[21] F.X. Liang, X.Y. Zhao, J.J. Jiang, J.G. Hu, W.Q. Xie, J. Lv, Z.X. Zhang, D. Wu, L.B. Luo,Small (2019), 1903831.
[22] C. Xie, B. Nie, L.H. Zeng, F.X. Liang, M.Z. Wang, L.B. Luo, M. Feng, Y.Q. Yu, C.Y. Wu, Y. Wu, S.H. Yu, ACS Nano 8 (2014) 4015–4022.
[23] H.A. Chaliyawala, A. Ray, R.K. Pati, I. Mukhopadhyay,Opt. Mater. 73 (2017), 449e458.

[24] H. Chaliyawala, N. Aggarwal, Z. Purohit, R. Patel, G. Gupta, A. Jaffre, S.L. Gall, A. Ray, I. Mukhopadhyay,Nanotechnology 31 (2020), 225208.
[25] S. Hao, J.W. Zeng, T. Xu, X. Cong, C.Y. Wang, C.C. Wu, Y.J. Wang, X.W. Liu, T.J. Cao, G.X. Su, L.X. Jia, Z.T. Wu, Q. Lin, L.L. Zhang, S.N. Yan, M.F. Guo, Z.L. Wang, P.H. Tan, L.T. Sun, Z.H. Ni, S.J. Liang, X.Y. Cui, F. Miao,Adv. Funct. Mater. 28 (2018), 1803746.
[26] H.F. Ma, P. Chen, B. Li, J. Li, R.Q. Ai, Z.W. Zhang, G.Z. Sun, K.K. Yao, Z.Y. Lin, B. Zhao, R.X. Wu, X.W. Tang, X.D. Duan, X.F. Duan, Nano Lett. 18 (2018) 3523–3529.
[27] L. Fu, D.B. Hu, R.G. Mendes, M.H. Rummeli, Q. Dai, B. Wu, L. Fu, Y.Q. Liu, ACS Nano 12 (2018) 9405–9411.
[28] J.Q. Liu, Y. Gao, G.A. Wu, X.W. Tong, C. Xie, L.B. Luo, L. Liang, Y.C. Wu, ACS Appl. Mater. Interfaces 10 (2018) 27850–27857.
[29] C. Yim, N. McEvoy, S. Riazimehr, D.S. Schneider, F. Gity, S. Monaghan, P.K. Hurley, M.C. Lemme, G.S. Duesberg, Nano Lett. 18 (2018) 1794–1800.
[30] L. Wang, S.J. He, K.Y. Wang, H.H. Luo, J.G. Hu, Y.Q. Yu, C. Xie, C.Y. Wu, L.B. Luo,Nanotechnology 29 (2018), 505203.
[31] X.W. Tong, Z.X. Zhang, D. Wang, L.B. Luo, C. Xie, Y.C. Wu, J. Mater. Chem. C 7 (2019) 863–870.
[32] J. Yao, Z.X. Deng, Z.Q. Zheng, G.W. Yang, ACS Appl. Mater. Interfaces 8 (2016) 20872–20879.
[33] X.W. Tong, W.Y. Kong, Y.Y. Wang, J.M. Zhu, L.B. Luo, Z.H. Wang, ACS Appl. Mater. Interfaces 9 (2017) 18977–18985.
[34] A. Rose, Concepts in Photoconductivity and Allied Problems, Krieger, New York, 1978.
[35] K.T. Fountaine, W.S. Whitney, H.A. Atwater,J. Appl. Phys. 116 (2014), 153106.
[36] S. Mokkapati, D. Saxena, H.H. Tan, C. Jagadish, Sci. Rep. 5 (2015) 15339.
[37] B. Wang, P.W. Leu, Opt. Lett. 37 (2012) 3756–3758.
[38] J.M. Liu, Photonic Devices, Cambridge University Press, Cambridge, 2005.
[39] L.B. Luo, J.J. Chen, M.Z. Wang, H. Hu, C.Y. Wu, Q. Li, L. Wang, J.A. Huang, F.X. Liang, Adv. Funct. Mater. 24 (2014) 2794–2800.
[40] X.M. Li, M. Zhu, M.D. Du, Z. Lv, L. Zhang, Y.C. Li, Y. Yang, T.T. Yang, X. Li, K.L. Wang, H.W. Zhu, Y. Fang, Small 12 (2016) 595–601.
[41] R.K. Chowdhury, R. Maiti, A. Ghorai, A. Midya, S.K. Ray, Nanoscale 8 (2016) 13429–13436.
[42] C. Xie, L.H. Zeng, Z.X. Zhang, Y.H. Tsang, L.B. Luo, J.H. Lee, Nanoscale 10 (2018) 15285–15293.
[43] J.D. Yao, J.M. Shao, Y.X. Wang, Z.R. Zhao, G.W. Yang, Nanoscale 7 (2015) 12535–12541.
[44] P. Lv, X.J. Zhang, X.W. Zhang, W. Deng, J.S. Jie, IEEE Electr. Device L. 34 (2013) 1337–1339.
[45] J. Mao, Y.Q. Yu, L. Wang, X.J. Zhang, Y.M. Wang, Z.B. Shao, J.S. Jie,Adv. Sci. 3 (2016), 1600018.
[46] L. Wang, J.S. Jie, Z.B. Shao, Q. Zhang, X.H. Zhang, Y.M. Wang, Z. Sun, S.T. Lee, Adv. Funct. Mater. 25 (2015) 2910–2919.
[47] X. An, F. Liu, Y.J. Jung, S. Kar, Nano Lett. 13 (2013) 909–916.
[48] L. Li, H.Y. Chen, Z.M. Fang, X.Y. Meng, C.T. Zuo, M.L. Lv, Y.Z. Tian, Y. Fang, Z. Xiao, C.X. Shan, Z.G. Xiao, Z.W. Jin, G.Z. Shen, L. Shen, L.M. Ding,Adv. Mater. 32 (2020), 1907257.
[49] L.H. Zeng, M.Z. Wang, H. Hu, B. Nie, Y.Q. Yu, C.Y. Wu, L. Wang, J.G. Hu, C. Xie, F.X. Liang, L.B. Luo, ACS Appl. Mater. Interfaces 5 (2013) 9362–9366.

Biography

Dr. Lin-Bao Luo received Ph. D. Degree from Department of Physics and Materials Sciences, City University of Hong Kong under the guidance of Prof. Shuit-Tong Lee in 2009. After spending one and half years at the same group as a research associate, he joined the College of Electronic Sciences and Applied Physics, Hefei University of Technology, where he is now a full professor of applied physics. He has published more than 180 peer referred journals including *IEEE TED*, *Adv. Mater.*, *Laser & Photonics Rev.*, *Adv. Funct. Mater.*, *Nano Lett.*, with a total citation of 6500 and an H-index of 47. His research interest mainly focuses on high-performance optoelectronic and electronic devices application including photodetectors (UV light, NIR), photovoltaic devices, and non-volatile memory devices etc. He has been invited to deliver lecture for more than 50 times in both domestic and international conferences.